Supporting Information for

Diffusive buckling fronts in lattice-based metamaterials

Jochem G. Meijer, Faadil H. Shaik, Victoria V. McDermott, and Heinrich M. Jaeger

Corresponding Author: Jochem G. Meijer
E-mail: jgmeijer@uchicago.edu

This PDF file includes:

Figs. S1 to S5
Legends for Movies S1 to S4
SI References

Other supporting materials for this manuscript include the following:

Movies S1 to S4

List of supplementary movies

- **Movie S1. Front view of two simple cubic lattices under compression showing local (left) and global (right) buckling, corresponding to Fig. 1*B*. Timestep indicates passed real time.**

- **Movie S2. Front- and side view of a simple cubic lattice under compression showing non-uniform local buckling and the formation of a domain wall (see Fig. 1*E*). Timestep indicates passed real time.**

- **Movie S3. 2D lattice structure under compression, corresponding to Fig. 5. First panel: Raw experimental data for a regular lattice. Remaining panels: Overlayed nodal rotation for the (second panel) regular lattice, (third panel) irregular lattice, and (last panel) heterogeneous lattice. For the irregular lattice bonds within the two red regions indicated in Fig. 5*E* have been randomly displaced. Timestep indicates passed real time.**

- **Movie S4. 2D simulations corresponding to different cases shown in Fig. 5.**

I - Domain walls in larger lattice structures

As addressed in the main text, all nodes have two rotation axes that are perpendicular to the compression direction, resulting in four possible rotation directions that can be triggered by the buckling instability. Since during buckling the angles bifurcate, different layers of the cubic lattice might arbitrarily choose a different orientation as compared to its adjacent layers. Uniform local buckling (strong coupling; all layers have the same orientation) gives way to non-uniformly buckled configurations (weak coupling), with domain walls between regions corresponding to different final states, see Fig. 1*E* in the main text. When looked from the front we see a change in orientation of the pattern-formation at different depths during local buckling. The side view clearly indicates that one layer has a different orientation as compared to the other three (green regions), which are separated by a domain wall (red region), that are bonds connecting these layers experiencing torsion.

One could now argue that given a large enough system, and assuming that the initial instabilities are triggered at the lesser confined edges, lattices with a stronger coupling between layers, i.e., those with thicker bonds, might eventually also show domain walls. To test this, we take the design of the cubic lattice indicated by the pink box in Fig. S1*A* and extend it in one direction, creating a 10x5x5 lattice, as shown in Fig. S1*B*. Whereas the front view does not clearly show the arising non-uniform pattern-formation during compression for this structure (left image), the side view clearly indicates the different orientation of the five layers on the left and on the right (green regions), separated again by a domain wall (red region). Apart from increasing the distance between the nucleation sides of the instabilities that then travel inwards through the lattice, one could also experiment by locally weakening the bonds connecting different layers by making them shorter, thinner or by using a material that is generally less stiff. The latter are future research directions that have not been explored yet.

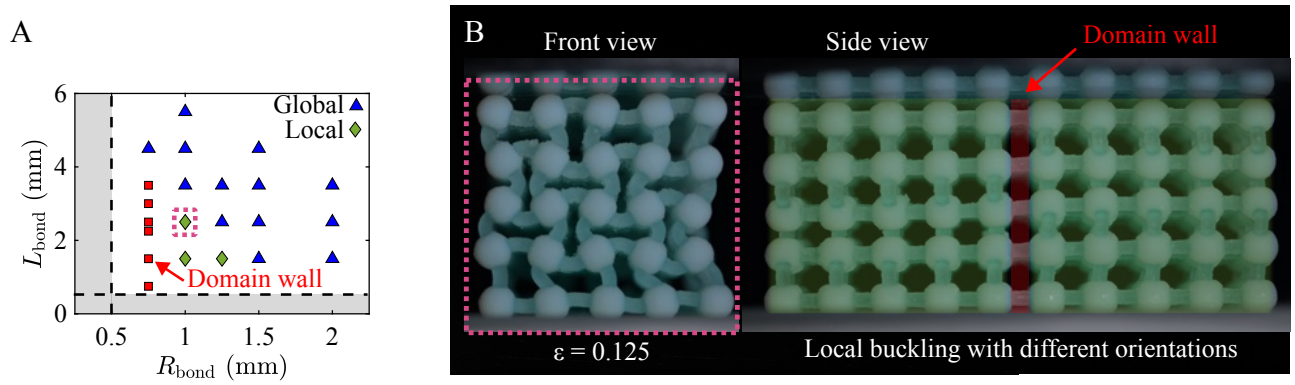

Fig. S1. Domain walls in extended lattices. (*A*) Parameter space in terms of bond length and bond radius indicating the cubic lattices (red squares) that show the formation of a domain wall during local buckling. (*B*) Front- and side view of a compressed 10x5x5 lattice structure with $R_{\mathrm{node}} = 2.5\,\mathrm{mm}$, $R_{\mathrm{bond}} = 1\,\mathrm{mm}$, and $L_z = 30\,\mathrm{mm}$. Although strongly coupled when compared to (a) (see pink box), increasing the distance between the nucleation sides of the instabilities (the lesser confined edges), domain walls can also emerge in these systems (red region).

II - The dynamic buckling equations

In this section we provide a detailed derivation of the dynamic buckling equations for both uniaxial and isotropic compression. We follow the line of thought as introduced on the main text, by modelling the interaction of the nodes through harmonic springs with different energies associated to them. Additionally we assume that all bonds dissipate energy depending on the angular velocities and neglect inertial effects. As mentioned in the main text we perform a coordinate transformation in line with the experimental observation on local buckling, assuming counter-rotation of neighbouring nodes that are in-plane. Angles perpendicular to this plane will be aligned uniformly. Transformation rules between both rotation basis are laid out below, as well as their affect on the overall structure of the dynamic buckling equations.

Uniaxial compression. Starting the derivation by developing a discrete model, we consider the following energy contributions for bending, shearing, torsion, compression, as well as two Rayleigh dissipation functions, respectively:

$$
\begin{aligned}
E_b &= \frac{1}{2}k_b \sum_{i,j,k} \left[\theta_{i,j,k} + \theta_{i+1,j,k}\right]^2 + \left[\theta_{i,j,k} + \theta_{i,j,k+1}\right]^2 + \left[\phi_{i,j,k} + \phi_{i,j+1,k}\right]^2 + \left[\phi_{i,j,k} + \phi_{i,j,k+1}\right]^2, \\
E_s &= \frac{1}{2}k_s \left(\frac{L_{\mathrm{bond}}}{2}\right)^2 \sum_{i,j,k} \left[\theta_{i,j,k} - \theta_{i+1,j,k}\right]^2 + \left[\theta_{i,j,k} - \theta_{i,j,k+1}\right]^2 + \left[\phi_{i,j,k} - \phi_{i,j+1,k}\right]^2 + \left[\phi_{i,j,k} - \phi_{i,j,k+1}\right]^2, \\
E_t &= \frac{1}{2}k_t \sum_{i,j,k} \left[\theta_{i,j,k} - \theta_{i,j+1,k}\right]^2 + \left[\phi_{i,j,k} - \phi_{i+1,j,k}\right]^2, \\
E_c &= -FL_{\mathrm{bond}} \sum_{i,j,k} \left[1 - \cos\theta_{i,j,k}\cos\phi_{i,j,k}\right], \\
\mathcal{F}_\theta &= \frac{1}{2}c_{\mathrm{disp}} \sum_{i,j,k} \dot{\theta}_{i,j,k}^2, \\
\mathcal{F}_\phi &= \frac{1}{2}c_{\mathrm{disp}} \sum_{i,j,k} \dot{\phi}_{i,j,k}^2.
\end{aligned}
$$

The coefficients are related to material properties as discussed in the main text. In short, $k_b = E_{\mathrm{bond}}I_{\mathrm{bond}}/L_{\mathrm{bond}}$, $k_s = \kappa G_{\mathrm{bond}}A_{\mathrm{bond}}/L_{\mathrm{bond}} = \frac{1-\zeta}{\zeta}G_{\mathrm{bond}}A_{\mathrm{bond}}R_{\mathrm{bond}}/L_{\mathrm{bond}}^2$, $k_t = G_{\mathrm{bond}}J_{\mathrm{bond}}/_{\mathrm{bond}}L$, $F = N^2E_{\mathrm{eff}}A_{\mathrm{bond}}\epsilon = N^2k_cL_{\mathrm{bond}}^2\epsilon$, with $k_c = E_{\mathrm{eff}}A_{\mathrm{bond}}/L_{\mathrm{bond}}$. The area and polar moments in inertia are $I_{\mathrm{bond}} = \pi R_{\mathrm{bond}}^4/4$ and $J_{\mathrm{bond}} = \pi R_{\mathrm{bond}}^4/2$.

We now consider potential energy $U = E_b + E_s + E_t + E_c$ and evaluate the simplified Lagrangian formulations $\partial_{\theta_{i,j,k}}(E_b + E_s + E_c + E_t) + \partial_{\dot{\theta}_{i,j,k}}\mathcal{F}_\theta = 0$, as well as $\partial_{\phi_{i,j,k}}(E_b + E_s + E_c + E_t) + \partial_{\dot{\phi}_{i,j,k}}\mathcal{F}_\phi = 0$. The derivatives read:

$$
\begin{aligned}
\partial_{\theta_{i,j,k}}U = {} & k_b\left[4\theta_{i,j,k} + \theta_{i+1,j,k} + \theta_{i-1,j,k} + \theta_{i,j,k+1} + \theta_{i,j,k-1}\right] \\
& + k_s\left(L_{\mathrm{bond}}/2\right)^2\left[4\theta_{i,j,k} - \theta_{i+1,j,k} - \theta_{i-1,j,k} - \theta_{i,j,k+1} - \theta_{i,j,k-1}\right] \\
& + k_t\left[2\theta_{i,j,k} - \theta_{i,j+1,k} - \theta_{i,j-1,k}\right] \\
& - FL_{\mathrm{bond}}\sin\theta_{i,j,k}\cos\phi_{i,j,k},
\end{aligned}
$$

$$
\begin{aligned}
\partial_{\phi_{i,j,k}}U = {} & k_b\left[4\phi_{i,j,k} + \phi_{i,j+1,k} + \phi_{i,j-1,k} + \phi_{i,j,k+1} + \phi_{i,j,k-1}\right] \\
& + k_s\left(L_{\mathrm{bond}}/2\right)^2\left[4\phi_{i,j,k} - \phi_{i,j+1,k} - \phi_{i,j-1,k} - \phi_{i,j,k+1} - \phi_{i,j,k-1}\right] \\
& + k_t\left[2\phi_{i,j,k} - \phi_{i+1,j,k} - \phi_{i-1,j,k}\right] \\
& - FL_{\mathrm{bond}}\sin\phi_{i,j,k}\cos\theta_{i,j,k},
\end{aligned}
$$

Eventually, we obtain two discrete equations as follows:

$$
\begin{aligned}
c_{\mathrm{disp}}\dot{\theta}_{i,j,k} = {} & -k_b\left[4\theta_{i,j,k} + \theta_{i+1,j,k} + \theta_{i-1,j,k} + \theta_{i,j,k+1} + \theta_{i,j,k-1}\right] \\
& - k_s\left(L_{\mathrm{bond}}/2\right)^2\left[4\theta_{i,j,k} - \theta_{i+1,j,k} - \theta_{i-1,j,k} - \theta_{i,j,k+1} - \theta_{i,j,k-1}\right] \\
& - k_t\left[2\theta_{i,j,k} - \theta_{i,j+1,k} - \theta_{i,j-1,k}\right] \\
& + FL_{\mathrm{bond}}\sin\theta_{i,j,k}\cos\phi_{i,j,k},
\end{aligned}
$$

$$
\begin{aligned}
c_{\mathrm{disp}}\dot{\phi}_{i,j,k} = {} & -k_b\left[4\phi_{i,j,k} + \phi_{i,j+1,k} + \phi_{i,j-1,k} + \phi_{i,j,k+1} + \phi_{i,j,k-1}\right] \\
& - k_s\left(L_{\mathrm{bond}}/2\right)^2\left[4\phi_{i,j,k} - \phi_{i,j+1,k} - \phi_{i,j-1,k} - \phi_{i,j,k+1} - \phi_{i,j,k-1}\right] \\
& - k_t\left[2\phi_{i,j,k} - \phi_{i+1,j,k} - \phi_{i-1,j,k}\right] \\
& + FL_{\mathrm{bond}}\sin\phi_{i,j,k}\cos\theta_{i,j,k}.
\end{aligned}
$$

Next, we approximate the discrete differences by continuous functions through Taylor expansions, approaching the continuum limit. As a consequence:

$$\theta_{i+1,j,k} + \theta_{i-1,j,k} - 2\theta_{i,j,k} \to L_{\text{bond}}^2 \frac{\partial^2 \theta}{\partial x^2},\ \theta_{i,j+,k} + \theta_{i,j-1,k} - 2\theta_{i,j,k} \to L_{\text{bond}}^2 \frac{\partial^2 \theta}{\partial y^2},\ \theta_{i,j,k+1} + \theta_{i,j,k-1} - 2\theta_{i,j,k} \to L_{\text{bond}}^2 \frac{\partial^2 \theta}{\partial z^2},$$
$$\phi_{i+1,j,k} + \phi_{i-1,j,k} - 2\phi_{i,j,k} \to L_{\text{bond}}^2 \frac{\partial^2 \phi}{\partial x^2},\ \phi_{i,j+1,k} + \phi_{i,j-1,k} - 2\phi_{i,j,k} \to L_{\text{bond}}^2 \frac{\partial^2 \phi}{\partial y^2},\ \phi_{i,j,k+1} + \phi_{i,j,k-1} - 2\phi_{i,j,k} \to L_{\text{bond}}^2 \frac{\partial^2 \phi}{\partial z^2}.$$

Additionally, assuming small angles we approximate that $\sin\theta\cos\phi \approx \left(\theta - \theta^3/6\right)\left(1 - \phi^2/2\right) \approx \theta - \theta^3/6 - \theta\phi^2/2$ and $\sin\phi\cos\theta \approx \left(\phi - \phi^3/6\right)\left(1 - \theta^2/2\right) \approx \phi - \phi^3/6 - \phi\theta^2/2$.

Combining and rewriting yields

$$c_{\text{disp}}\dot{\theta} = \left(k_s L_{\text{bond}}^2/4 - k_b\right) L_{\text{bond}}^2 \nabla_{xz}^2 \theta + k_t L_{\text{bond}}^2 \frac{\partial^2 \theta}{\partial y^2} + F L_{\text{bond}} \theta - 8k_b\theta - \frac{F L_{\text{bond}}}{6}\theta^3 - \frac{F L_{\text{bond}}}{2}\theta\phi^2,$$
$$c_{\text{disp}}\dot{\phi} = \left(k_s L_{\text{bond}}^2/4 - k_b\right) L_{\text{bond}}^2 \nabla_{yz}^2 \phi + k_t L_{\text{bond}}^2 \frac{\partial^2 \phi}{\partial x^2} + F L_{\text{bond}} \phi - 8k_b\phi - \frac{F L_{\text{bond}}}{6}\phi^3 - \frac{F L_{\text{bond}}}{2}\phi\theta^2.$$

Finally, we can obtain Eq. 3 & 4 from the main text:

$$\dot{\theta} = D_{xz}\nabla_{xz}^2\theta + D_y \frac{\partial^2 \theta}{\partial y^2} + f(\theta, \phi),$$
$$\dot{\phi} = D_{yz}\nabla_{yz}^2\phi + D_x \frac{\partial^2 \phi}{\partial x^2} + g(\theta, \phi),$$

with $D_{xz} = D_{yz} = \left(k_s L_{\text{bond}}^2/4 - k_b\right) L_{\text{bond}}^2/c_{\text{disp}}$ and $D_y = D_x = k_t L_{\text{bond}}^2/c_{\text{disp}}$ the diffusivity constants in the xz- and yz-planes, and y- and x-directions, respectively. Also, $\nabla_{xz}^2 = \partial^2/\partial x^2 + \partial^2/\partial z^2$ and $\nabla_{yz}^2 = \partial^2/\partial y^2 + \partial^2/\partial z^2$, and the forcing terms read:

$$f(\theta, \phi) = \mathcal{C}_\theta \left[1 - \frac{8k_b}{F L_{\text{bond}}} - \frac{\theta^2}{6} - \frac{\phi^2}{2}\right]\theta,$$
$$g(\theta, \phi) = \mathcal{C}_\phi \left[1 - \frac{8k_b}{F L_{\text{bond}}} - \frac{\phi^2}{6} - \frac{\theta^2}{2}\right]\phi,$$

where $\mathcal{C}_\theta = \mathcal{C}_\phi = F L_{\text{bond}}/c_{\text{disp}}$.

Isotropic compression. We can repeat the derivation considering also rotation in the xy-plane, which we define as ψ. Additionally, we can apply isotropic compression with forces in the three principle directions, namely F_x, F_y, and F_z for a more generalized description. Without providing the derivation, the obtained system of equations becomes:

$$\dot{\theta} = D_{xz}\nabla_{xz}^2\theta + D_y \frac{\partial^2 \theta}{\partial y^2} + f(\theta, \phi, \psi),$$
$$\dot{\phi} = D_{yz}\nabla_{yz}^2\phi + D_x \frac{\partial^2 \phi}{\partial x^2} + g(\theta, \phi, \psi),$$
$$\dot{\psi} = D_{xy}\nabla_{xy}^2\psi + D_z \frac{\partial^2 \psi}{\partial z^2} + h(\theta, \phi, \psi),$$

with $D_{xz} = D_{yz} = D_{xy} = \left(k_s L_{\text{bond}}^2/4 - k_b\right) L_{\text{bond}}^2/c_{\text{disp}}$ and $D_y = D_x = D_z = k_t L_{\text{bond}}^2/c_{\text{disp}}$ the diffusivity constants in the xz-, yz-, and xy-planes, and y-, x-, and z-directions, respectively. Also, $\nabla_{xz}^2 = \partial^2/\partial x^2 + \partial^2/\partial z^2$, $\nabla_{yz}^2 = \partial^2/\partial y^2 + \partial^2/\partial z^2$, and $\nabla_{xy}^2 = \partial^2/\partial x^2 + \partial^2/\partial y^2$. The forcing terms read:

$$f(\theta, \phi, \psi) = \mathcal{C}_\theta \left[1 - \frac{8k_b}{(F_x + F_z) L_{\text{bond}}} - \frac{\theta^2}{6}\right]\theta - \frac{L_{\text{bond}}}{2}\left[F_x\psi^2 + F_z\phi^2\right]\theta,$$
$$g(\theta, \phi, \psi) = \mathcal{C}_\phi \left[1 - \frac{8k_b}{(F_y + F_z) L_{\text{bond}}} - \frac{\phi^2}{6}\right]\phi - \frac{L_{\text{bond}}}{2}\left[F_y\psi^2 + F_z\theta^2\right]\phi,$$
$$h(\theta, \phi, \psi) = \mathcal{C}_\psi \left[1 - \frac{8k_b}{(F_x + F_y) L_{\text{bond}}} - \frac{\phi^2}{6}\right]\psi - \frac{L_{\text{bond}}}{2}\left[F_y\phi^2 + F_x\theta^2\right]\psi,$$

where $\mathcal{C}_\theta = (F_x + F_z) L_{\text{bond}}/c_{\text{disp}}$, $\mathcal{C}_\phi = (F_y + F_z) L_{\text{bond}}/c_{\text{disp}}$, and $\mathcal{C}_\psi = (F_x + F_y) L_{\text{bond}}/c_{\text{disp}}$. Taking $F_x = F_y = \psi = 0$ yields the uniaxial compression case for $F_z = F$.

Derivation in the co-rotating reference frame. As mentioned above, the derivation is performed in the counter-rotating reference frame with counter-rotating neighbours in-plane and aligned rotation in the perpendicular direction. The following transformation rules between 'global' co-rotation ($\theta^\star$) and 'local' counter-rotation (θ) hold:

$$\theta^\star_{i,j,k} = (-1)^{i+k}\,\theta_{i,j,k}, \quad \phi^\star_{i,j,k} = (-1)^{j+k}\,\phi_{i,j,k}, \quad \psi^\star_{i,j,k} = (-1)^{i+j}\,\psi_{i,j,k}.$$

If we change to the co-rotating frame of reference (which more resembles the nodal rotation corresponding to global buckling, see Fig. 1*C* in the main text), the above equations become:

$$\begin{aligned}
\dot{\theta}^\star =& D^\star_{xz}\nabla^2_{xz}\theta^\star + D_y\frac{\partial^2\theta^\star}{\partial y^2} + f(\theta^\star,\phi^\star,\psi^\star),\\
\dot{\phi}^\star =& D^\star_{yz}\nabla^2_{yz}\phi^\star + D_x\frac{\partial^2\phi^\star}{\partial x^2} + g(\theta^\star,\phi^\star,\psi^\star),\\
\dot{\psi}^\star =& D^\star_{xy}\nabla^2_{xy}\psi^\star + D_z\frac{\partial^2\psi^\star}{\partial z^2} + h(\theta,\phi^\star,\psi^\star),
\end{aligned}$$

with $D^\star_{xz} = D^\star_{yz} = D^\star_{xy} = \left(k_b - k_s L^2_{\text{bond}}/4\right) L^2_{\text{bond}}/c_{\text{disp}}$. The forcing terms read:

$$\begin{aligned}
f(\theta^\star,\phi^\star,\psi^\star) =& \mathcal{C}_\theta\left[1 - \frac{8k_sL^2_{\text{bond}}}{(F_x+F_z)\,L_{\text{bond}}} - \frac{\theta^{\star\,2}}{6}\right]\theta^\star - \frac{L_{\text{bond}}}{2}\left[F_x\psi^{\star\,2} + F_z\phi^{\star\,2}\right]\theta^\star,\\
g(\theta^\star,\phi^\star,\psi^\star) =& \mathcal{C}_\phi\left[1 - \frac{8k_sL^2_{\text{bond}}}{(F_y+F_z)\,L_{\text{bond}}} - \frac{\phi^{\star\,2}}{6}\right]\phi^\star - \frac{L_{\text{bond}}}{2}\left[F_y\psi^{\star\,2} + F_z\theta^{\star\,2}\right]\phi^\star,\\
h(\theta^\star,\phi^\star,\psi^\star) =& \mathcal{C}_\psi\left[1 - \frac{8k_sL^2_{\text{bond}}}{(F_x+F_y)\,L_{\text{bond}}} - \frac{\phi^{\star\,2}}{6}\right]\psi^\star - \frac{L_{\text{bond}}}{2}\left[F_y\phi^{\star\,2} + F_x\theta^{\star\,2}\right]\psi^\star.
\end{aligned}$$

In the main text we argue that we transition from global to local buckling when $k_b/(k_sL^2_{\text{bond}}) = 1$, which is a direct consequence for the case when $D_\theta = D^\star_\theta$. This is also criteria that is the bases of the derivation of Eq. 1 in the main text.

Buckling plane selection. Here we analytically show that the selection of a buckling plane will persist, *i.e.*, $\theta \neq 0$ and $\phi = 0$ or vice versa, for uniaxial compression. As stated in the main text, we assume a potential energy $V(\theta,\phi)$ for which $\partial V(\theta,\phi)/\partial\theta = -c_{\text{disp}}f(\theta,\phi) = 0$ and $\partial V(\theta,\phi)/\partial\phi = -c_{\text{disp}}g(\theta,\phi) = 0$ need to be satisfied. If both variables are non-zero, we can show they must be equal, hence $\theta^2 = \phi^2 = \xi^2$. Evaluating the terms in brackets of $f(\theta,\phi)$ or $g(\theta,\phi)$ then yields

$$\theta^2 = \phi^2 = \xi^2 = \frac{3\left(1 - \frac{8k_b}{FL_{\text{bond}}}\right)}{2}.$$

Integration of $f(\theta,\phi)$ and $g(\theta,\phi)$ results in a potential energy as

$$V(\theta,\phi) = -c_{\text{disp}}\mathcal{C}\left[\left(1 - \frac{8k_b}{FL_{\text{bond}}}\right)\frac{\theta^2+\phi^2}{2} - \frac{\theta^4+\phi^4}{24} - \frac{\theta^2\phi^2}{4}\right], \qquad [1]$$

with $\mathcal{C} = \mathcal{C}_\theta = \mathcal{C}_\phi$. The Hessian of this function reads

$$H \propto \begin{pmatrix} \frac{8k_b}{FL_{\text{bond}}} - 1 + \frac{\theta^2}{2} + \frac{\phi^2}{2} & \theta\phi \\ \theta\phi & \frac{8k_b}{FL_{\text{bond}}} - 1 + \frac{\phi^2}{2} + \frac{\theta^2}{2} \end{pmatrix}.$$

Let $\theta^2 = \phi^2 = \xi^2$, then

$$\begin{aligned}
a &= \frac{8k_b}{FL_{\text{bond}}} - 1 + \xi^2 = \frac{1}{2}\left[1 - \frac{8k_b}{FL_{\text{bond}}}\right],\\
b &= \theta\phi = \pm\xi^2 = \pm\frac{3}{2}\left[1 - \frac{8k_b}{FL_{\text{bond}}}\right].
\end{aligned}$$

Hence,

$$\det(H) \propto a^2 - b^2 = \frac{1}{4}\left[1 - \frac{8k_b}{FL_{\text{bond}}}\right]^2 - \frac{9}{4}\left[1 - \frac{8k_b}{FL_{\text{bond}}}\right]^2 = -2\left[1 - \frac{8k_b}{FL_{\text{bond}}}\right]^2 < 0.$$

Since $\det(H) < 0$ this resembles a saddle point, which is unstable. For the selection of a buckling plane (i.e., $\theta \neq 0$, $\phi = 0$ or vice versa) the Hessian is diagonal with positive diagonal elements. This represents a stable minimum and agrees with our experimental observations (see Fig. 1*B*).

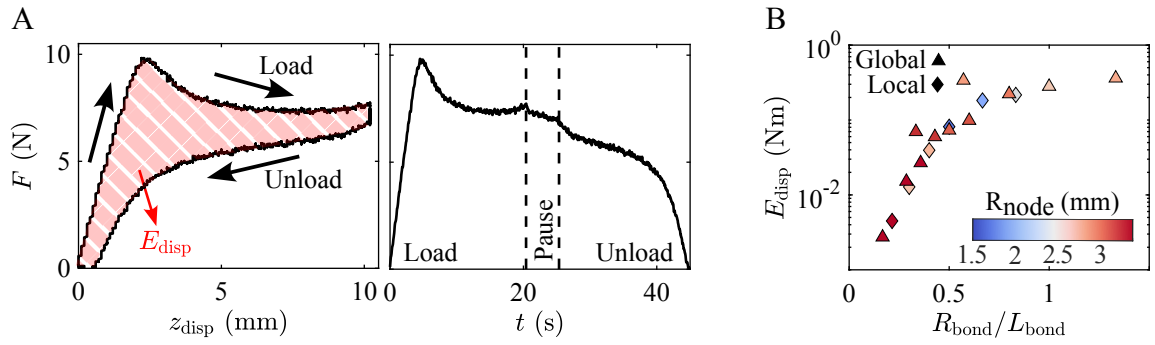

Fig. S2. Strain energy dissipation. (*A*) Force as a function of compression z_{disp} (left) and time (right) for a simple cubic lattice with $N = 5$, $R_{\mathrm{node}} = 2\,\mathrm{mm}$, $R_{\mathrm{bond}} = 1.25\,\mathrm{mm}$, and $L = 30\,\mathrm{mm}$. Between loading and unloading we pause for 5 s. The red shaded area with the force versus displacement loop defines the energy dissipated E_{disp} by the cubic lattice during one loading cycle. (*B*) Averaged dissipated energy E_{disp} as a function of bond radius over bond length for all designs over three loading cycles.

III - Strain energy dissipation dependence on lattice structure

Here we look into the energy that is being dissipated by the three-dimensional simple cubic lattices during one loading cycle. It allows us to quantify how sensitive the strain energy dissipation is with respect to the architecture of the lattice structure. Since the sizes of the cubic lattices are not hugely different and we always use the same crosshead speed during compression, variations in strain rate $\dot{\epsilon}$ are assumed to be negligible. The affect of strain rate on the loss modulus (or here the energy dissipated during one loading cycle) is beyond the scope of the current study.

The loading cycle consists out of a loading stage up to 0.3 strain with crosshead speed $v = 0.5\,\mathrm{mm\,s^{-1}}$, followed by a pause of 5 s, and subsequent unloading at the same speed. A typical force versus displacement curve is shown in Fig. S2*A*, as well as force versus time. After the linear response during loading the lattice buckles and weakens. During the pause, some energy is dissipated, reflecting the viscoelasticity in the 3D-printed material, and even more so during unloading. The mechanical work associated with the force-displacement cycle is calculated by integrating the force over displacement,

$$E = \int_{\delta} F(z)\,\mathrm{d}z,$$

where δ denotes the relevant loading or unloading path. During loading, the work input is

$$E_{\mathrm{load}} = \int_{0}^{z_{\mathrm{max}}} F_{\mathrm{load}}(z)\,\mathrm{d}z,$$

while during unloading it is given by

$$E_{\mathrm{unload}} = \int_{z_{\mathrm{max}}}^{0} F_{\mathrm{unload}}(z)\,\mathrm{d}z.$$

By construction, $E_{\mathrm{load}} > 0$ and $E_{\mathrm{unload}} < 0$. The dissipated energy, corresponding to the area enclosed by the force-displacement loop, is then $E_{\mathrm{disp}} = E_{\mathrm{load}} - |E_{\mathrm{unload}}|$. We define the dissipation ratio as $\eta = E_{\mathrm{disp}}/E_{\mathrm{load}} = 1 - |E_{\mathrm{unload}}|/E_{\mathrm{load}}$ (see Fig. 2*F* in the main text).

IV - Loading rate dependence on mechanical response, strain energy dissipation and nodal rotation dynamics

The mechanical response of a typical structure with $N = 5$, $R_{\mathrm{bond}} = 1\,\mathrm{mm}$, $R_{\mathrm{node}} = 2.5\,\mathrm{mm}$ and $L_{\mathrm{bond}} = 2.5\,\mathrm{mm}$ is shown here in Fig. S3*A*&*B* for crosshead velocities ranging from $0.02\,\mathrm{mm\,s^{-1}}$ to $50\,\mathrm{mm\,s^{-1}}$. Whereas the mechanical response seems to converge at low straining velocities, the larger the velocity becomes, the stiffer the structure gets. This is expected due to the viscoelastic nature of the polymers. Apart from the change in stiffness, also the critical strain at which buckling occurs shifts towards larger values as the compression speed is increased.

When unloading the structure after loading at $50\,\mathrm{mm\,s^{-1}}$ with the same velocity, the structure has dissipated some energy (see Fig. S3*C*). When determining the strain dissipation ratio as discussed in the main text we find a value of $\eta = 0.98$. This is significantly larger as compared to loading/unloading at a lower velocity (see Fig. 2*F* in the main text).

Although the mechanical response and the energy dissipation are highly dependent on the loading-rate, the most important feature for our study, namely the dynamics of the node rotations, remain unchanged upon proper normalisation. We show this in Fig. S3*D*&*E*. Fig. S3*D* shows experimental snapshots of the compression of the same lattice structure at different loading-rates at the same values of applied strain, exhibiting striking similarities. To quantify this, we look into the node rotations of the center nine nodes (as also done in Fig. 1*C* of the main text) in Fig. S3*E*. The upper plots show θ as a function of strain for the slow (left) and fast (right) compression. The lower plots shows their collapse when normalising strain with the corresponding value of the critical strain at which buckling occurs.

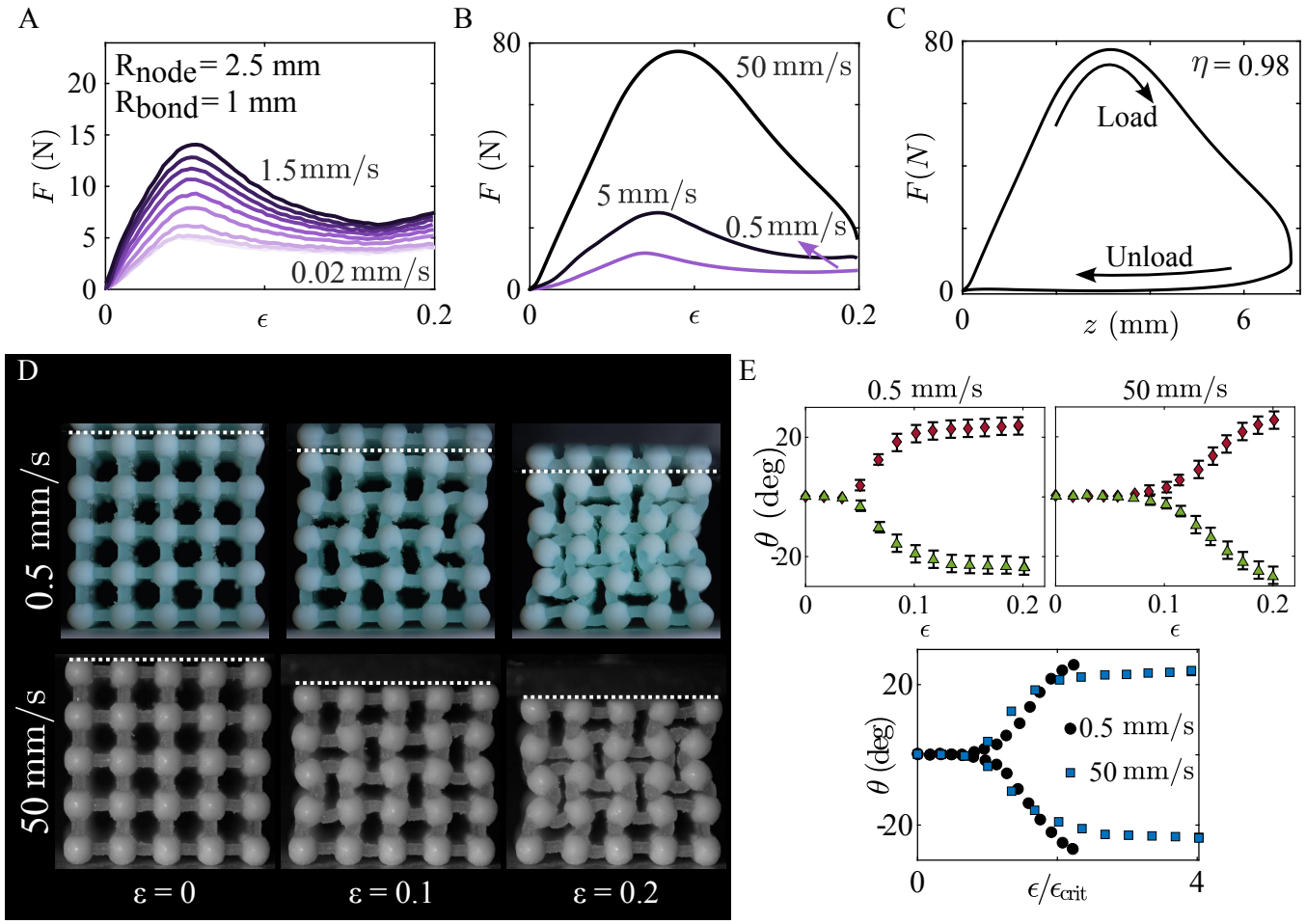

Fig. S3. (*A-B*) Force strain relationships of a typical structure with $N = 5$, $R_{\rm bond} = 1\,{\rm mm}$, $R_{\rm node} = 2.5\,{\rm mm}$ and $L_{\rm bond} = 2.5\,{\rm mm}$ at different crosshead velocities. Curves are averages of three repetitions. (*C*) Force versus displacement during a loading and unloading cycle of the same structure at $v_{\rm crosshead} = 50\,{\rm mm\,s^{-1}}$. The strain energy dissipation ratio is determined to be $\eta = 0.98$. (*D*) Experimental snapshots of the lattice structure during slow (top) and fast (bottom) compression. (*E*) Nodal rotations of the center nine nodes for the slow (top left) and fast (top right) compression. Bottom: Node rotations as a function of $\epsilon/\epsilon_{\rm crit}$.

V - Numerical implementation

In order to evaluate Eqs. 3 & 5 of the main text numerically we non-dimensionalize the system of equations. To repeat, we have

$$\partial_t\theta(\vec{x},t) = D_{xz}\left(\partial_x^2+\partial_z^2\right)\theta(\vec{x},t) + D_y\partial_y^2\theta(\vec{x},t) - \mathcal{R}\epsilon_{\rm crit}\theta(\vec{x},t) + \mathcal{R}\epsilon\theta(\vec{x},t) + \mathcal{R}\epsilon\frac{\theta(\vec{x},t)^3}{6} + \mathcal{R}\epsilon\frac{\theta(\vec{x},t)\phi(\vec{x},t)^2}{2},$$

$$\partial_t\phi(\vec{x},t) = D_{yz}\left(\partial_y^2+\partial_z^2\right)\phi(\vec{x},t) + D_x\partial_x^2\phi(\vec{x},t) - \mathcal{R}\epsilon_{\rm crit}\phi(\vec{x},t) + \mathcal{R}\epsilon\phi(\vec{x},t) + \mathcal{R}\epsilon\frac{\phi(\vec{x},t)^3}{6} + \mathcal{R}\epsilon\frac{\phi(\vec{x},t)\theta(\vec{x},t)^2}{2},$$

with $D_{xz} = D_{yz} = \left(k_s L_{\rm bond}^2/4 - k_b\right) L_{\rm bond}^2/c_{\rm disp}$, $D_y = D_x = k_t L_{\rm bond}^2/c_{\rm disp}$, and $\mathcal{R} = N^2 k_c L_{\rm bond}^2/c_{\rm disp}$. We then consider the following substitutions:

$$\tilde{t} = \frac{t}{\tau_{\rm diff}}, \quad \tilde{\vec{x}} = \frac{\vec{x}}{L_{\rm bond}}, \quad \tilde{\theta} = \frac{\theta}{\theta_{\rm max}}, \quad \tilde{\phi} = \frac{\phi}{\phi_{\rm max}},$$

where tildes denote dimensionless quantities. $\tau_{\rm diff}$ is the experimentally observed diffusion time scale, e.g., the time it takes in the experiments for diffusion to have propagated throughout the whole system. The latter is approximately 50 s for the case shown in Fig. 5 in the main text. $\theta_{\rm max} = \phi_{\rm max} = 40^\circ = \frac{2\pi}{9}{\rm rad}$ is the experimentally observed maximum node rotation during compression and also used as upper constraint in the simulations. Substitution then yields

$$\partial_{\tilde{t}}\tilde{\theta} = \frac{D_{xz}\tau_{\rm diff}}{L_{\rm bond}^2}\left(\partial_{\tilde{x}}^2+\partial_{\tilde{z}}^2\right)\tilde{\theta} + \frac{D_y\tau_{\rm diff}}{L_{\rm bond}^2}\partial_{\tilde{y}}^2\tilde{\theta} - \mathcal{R}\tau_{\rm diff}\epsilon_{\rm crit}\tilde{\theta} + \mathcal{R}\tau_{\rm diff}\epsilon\tilde{\theta} + \mathcal{R}\tau_{\rm diff}\epsilon\frac{\tilde{\theta}^3}{6\theta_{\rm max}^2} + \mathcal{R}\tau_{\rm diff}\epsilon\frac{\tilde{\theta}\tilde{\phi}^2}{2\phi_{\rm max}^2},$$

$$\partial_{\tilde{t}}\tilde{\phi} = \frac{D_{yz}\tau_{\rm diff}}{L_{\rm bond}^2}\left(\partial_{\tilde{y}}^2+\partial_{\tilde{z}}^2\right)\tilde{\phi} + \frac{D_x\tau_{\rm diff}}{L_{\rm bond}^2}\partial_{\tilde{x}}^2\tilde{\phi} - \mathcal{R}\tau_{\rm diff}\epsilon_{\rm crit}\tilde{\phi} + \mathcal{R}\tau_{\rm diff}\epsilon\tilde{\phi} + \mathcal{R}\tau_{\rm diff}\epsilon\frac{\tilde{\phi}^3}{6\phi_{\rm max}^2} + \mathcal{R}\tau_{\rm diff}\epsilon\frac{\tilde{\phi}\tilde{\theta}^2}{2\theta_{\rm max}^2}.$$

We obtain dimensionless groups

$$\tilde{D}_{xz} = \frac{D_{xz}\tau_{\rm diff}}{L_{\rm bond}^2}, \quad \tilde{D}_{yz} = \frac{D_{yz}\tau_{\rm diff}}{L_{\rm bond}^2}, \quad \tilde{D}_y = \frac{D_y\tau_{\rm diff}}{L_{\rm bond}^2}, \quad \tilde{D}_x = \frac{D_x\tau_{\rm diff}}{L_{\rm bond}^2}, \quad \tilde{\mathcal{R}} = \mathcal{R}\tau_{\rm diff}.$$

We numerically solve the dimensionless equations by standard finite, first order difference discretization of the second-order derivatives on a three-dimensional grid with $L_x = L_y = L_z = 50$ points and lattice spacing $dx = dy = dz = 1$. Time integration is performed using a forward (explicit) scheme and the time-step $dt \ll 1$ is kept small to ensure stability.

As initial conditions, we assume random initial perturbations of the order of 1% for both angles, as well as stronger Gaussian initial perturbations in line with experimental observations regarding their origin (the least confined edges); see Fig. 4*A*&*B* of the main text, respectivly. We also consider $\epsilon = \epsilon_0 + \dot{\epsilon}\tilde{t}$ - in line with the strain driven experiments - with an initial value for ϵ_0 that can be lower, equal to or larger than ϵ_{crit}, where typically $\epsilon_{\text{crit}} = 0.05$. The strain rate can be chosen such to match experiments, with $\dot{\epsilon} = 3 \times 10^{-3}\,\text{s}^{-1}$ as typical value for the case corresponding to Fig. 5 of the main text, resulting in $\tilde{\dot{\epsilon}} = \dot{\epsilon}\tau_{\text{diff}}$ in the dimensionless simulations.

Quantitive comparison to experiments.. In Fig. 5*C* in the main text we have compared the evolution of the buckling front between 2D experiments and simulations. Here we provide additional details regarding their quantitive agreement.

Fig. S4*A* corresponds to Fig. 5*C* of the main text showing the mean absolute angle normalised by $\theta_{\max} = 40^\circ = \frac{2\pi}{9}\text{rad}$ as a function of dimensionless and rescaled vertical postion $z^\star = 1 - \frac{z}{L(1-\epsilon)}$. Different symbols (experimet, left) and colours (simulation, right) correspond to instances in time at equal strain, with $\epsilon = [0.05, 0.1, 0.15, 0.2]$, respectively. The circles in the left plot of Fig. S4*A* correspond to $\epsilon = 0$.

For the simulations the system of equations simplifies due to the 2D approximation ($D_y = D_x = \phi = 0$), resulting in

$$\partial_{\tilde{t}}\tilde{\theta} = \frac{D_{xz}\tau_{\text{diff}}}{L^2_{\text{bond}}}\left(\partial^2_{\tilde{x}} + \partial^2_{\tilde{z}}\right)\tilde{\theta} - \mathcal{R}\tau_{\text{diff}}\epsilon_{\text{crit}}\tilde{\theta} + \mathcal{R}\tau_{\text{diff}}\epsilon\tilde{\theta} + \mathcal{R}\tau_{\text{diff}}\epsilon\frac{\tilde{\theta}^3}{6\theta^2_{\max}}.$$

As an initial condition we consider the experimental snapshot at $\epsilon = 0.05$. We now can match the representative curves of the evolving buckling fronts considering that the front takes the shape of a hyperbolic tangent (show in Suppl. Mat. Sec. XX) to determine the approximate values of $\tilde{D}_{xz} = \frac{D_{xz}\tau_{\text{diff}}}{L^2_{\text{bond}}}$ and $\tilde{\mathcal{R}} = \mathcal{R}\tau_{\text{diff}}$. The dashed lines in Fig. S4*A* fit $y = a\tanh\left[b\left(z^\star - c\right)\right] + d$ to the profiles (excluding the effect of the left-hand side boundaries) with c the center of the buckling front and $w_{10-90} = 2.2/b$ its 10%-to-90% width; see right plot of Fig. S4*A* for definitions. In Fig. S4*B* their numerical values are compared for the experiment (square) and simulation (circle). We find that the front width in the simulation is systematically smaller. An explanation for this might be the limited number of bonds in the 2D experiments. Apart from the center and the width, the slope between points in the left plot of Fig. S4*B* contains information regarding the velocity of the buckling front, as $\epsilon = \epsilon_0 + \dot{\epsilon}t$.

Eventually, values of the non-dimensional in-plane diffusion coefficient ($\tilde{D}_{xz}$) and reaction term ($\tilde{\mathcal{R}}$) are determined that provide a match between experiments and simulations, where $D_{xz}/L^2_{\text{bond}} = \mathcal{O}(1)$ and $\mathcal{R} = \mathcal{O}(1)$.

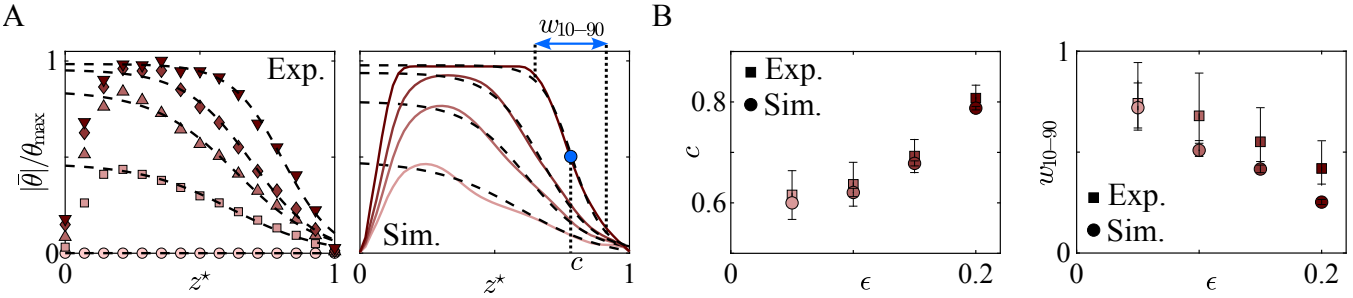

Fig. S4. (*A*) Normalized averages of the rotation angles as a function of rescaled vertical coordinate $z^\star$ at different instances in time (or strain), for crosshead speed $0.5\,\text{mm}\,\text{s}^{-1}$. The dashed lines correspond to fitted hyperbolic tangents. (*B* Obtained values of the center c and its 10%-to-90% width w_{10-90} for the experiment (squares) and simulation (circles). The slope of the left plot is representative for the front velocity since $\epsilon = \epsilon_0 + \dot{\epsilon}\tilde{t}$.)

VI - Additional lattice configurations

To investigate the affect of lattice design on the formation and evolution of the diffusive buckling fronts in the experimental 2D systems, we have fabricated similar designs as shown in Fig. 5 in the main text (here Fig. S5*A*) but with slightly different configurations. We then perform the same compression experiments as discussed in the main text with a crosshead velocity of $v_{\text{crosshead}} = 0.5\,\text{mm}\,\text{s}^{-1}$ to a target strain of $\epsilon = 0.2$. We then plot the lab-frame node rotations of all the nodes, overlayed on the experimental snapshot in Fig. S5.

In Fig. S5*B* we consider a staggered lattice where the bonds are aligned vertically in the direction of the uni-axial compression. Now, node rotations are still observed yet nodes within the same row co- instead of counter-rotate. Nonetheless, the counter-rotation of the nodes and the associated local buckling is still present, but now on the diagonals, parallel to the orientation of the bonds. Buckling still nucleates at the upper edges of the 2D lattice before propagating through the system, similar to the regular lattice, however the extend to which the lattice shrinks inwards during compression, e.g., the extend of its auxetic behaviour, reduces.

When rotating the staggered lattice the bonds align perpendicular the direction of the uni-axial compression, see Fig. S5*C*. Now, no bonds are sufficiently load-bearing to induce buckling and node rotations remain absent throughout the compression.

In the continuum models this corresponds to F_z (and hence $\mathcal{C}$) in Eq. 4 of the main text to remain sufficiently small, that the reaction terms remain negative (sinks) indefinitely.

Lastly, when allowing for a higher degree of connectivity in a triangular lattice (see Fig. S5 *D*), node rotations are largely suppressed as the nodes become too constrained. Rotation of the nodes only occurs at the lesser confined boundaries.

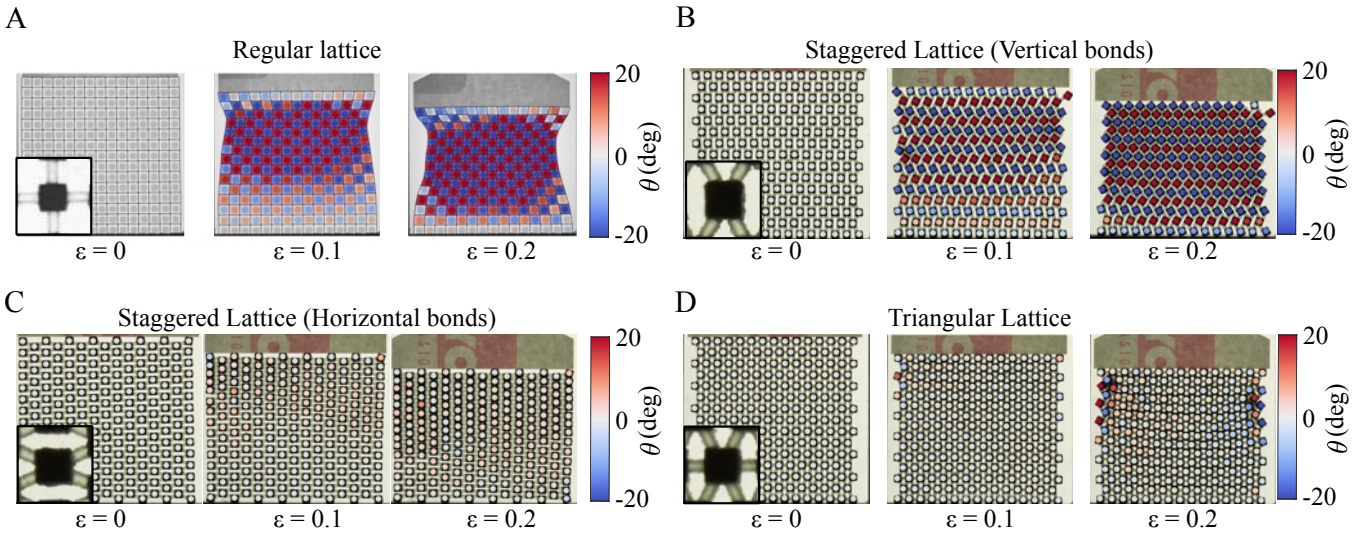

Fig. S5. Lab-frame node rotation of 2D lattices similar to those in Fig. 5 in the main text for a (*A*) regular lattice, (*B*) staggered lattice with vertical bonds, (*C*) staggered lattice with horizontal bonds, and (*D*) triangular lattice.

VII - Inertial effects

In the main text we have neglected inertial effects given the small masses of the nodes and the low strain rates. Here, we explore how the dynamics are affected if inertia was significant. We apply the same methodology as above for the case of uniaxial compression. Apart from potential energy U we assume an additional contribution that represents the kinetic energy of the nodes, *i.e.*, $T = J_I\dot{\theta}^2/2$, with J_I the moment of inertia. Then, $L = T - U$ and we evaluate $\mathrm{d}/\mathrm{d}t\left(\partial_{\dot{\theta}_{i,j,k}} L\right) - \partial_{\theta_{i,j,k}} L + \partial_{\dot{\theta}_{i,j,k}} \mathcal{F} = 0 \rightarrow \mathrm{d}/\mathrm{d}t\left(\partial_{\dot{\theta}_{i,j,k}} T\right) + \partial_{\theta_{i,j,k}} U + \partial_{\dot{\theta}_{i,j,k}} \mathcal{F} = 0$ (equivalently for $\phi_{i,j,k}$).

Follow the same line of thought as above the final results read

$$J_I\ddot{\theta} + c_{\mathrm{disp}}\dot{\theta} = \left(k_s L_{\mathrm{bond}}^2 - k_b\right) L_{\mathrm{bond}}^2 \nabla_{xz}^2\theta + k_t L_{\mathrm{bond}}^2 \frac{\partial^2\theta}{\partial y^2} + f(\theta,\phi),$$

$$J_I\ddot{\phi} + c_{\mathrm{disp}}\dot{\phi} = \left(k_s L_{\mathrm{bond}}^2 - k_b\right) L_{\mathrm{bond}}^2 \nabla_{yz}^2\phi + k_t L_{\mathrm{bond}}^2 \frac{\partial^2\phi}{\partial x^2} + g(\theta,\phi).$$

The forcing terms remain unchanged, apart from a prefactor. The above set of equations now resemble wave equations. More specifically, they are non-linear Klein-Gordon equations with damping. Equivalent forms for similar systems have been derived in earlier works (1–6).

Topological defects. We assume buckling in only one angle and no damping to simplify the equation:

$$J_I\ddot{\theta} = \left(k_s L_{\mathrm{bond}}^2 - k_b\right) L_{\mathrm{bond}}^2 \nabla_{xz}^2\theta + k_t L_{\mathrm{bond}}^2 \frac{\partial^2\theta}{\partial y^2} + N^2 k_c L_{\mathrm{bond}}^2 \epsilon \left[1 - \frac{\epsilon_{\mathrm{crit}}}{\epsilon} - \frac{\theta^2}{6}\right]\theta.$$

Now we perform a coordinate substitution such that:

$$\tilde{t} = \sqrt{\frac{\gamma}{J_I}}t, \quad \tilde{x} = \frac{\sqrt{\gamma}}{L_{\mathrm{bond}}\sqrt{k_s L_{\mathrm{bond}}^2 - k_b}}x, \quad \tilde{y} = \frac{\sqrt{\gamma}}{L_{\mathrm{bond}}\sqrt{k_t}}y, \quad \tilde{z} = \frac{\sqrt{\gamma}}{L_{\mathrm{bond}}\sqrt{k_s L_{\mathrm{bond}}^2 - k_b}}z, \quad \Theta = \frac{\theta}{\sqrt{-\frac{6\gamma}{F L_{\mathrm{bond}}}}},$$

with $\gamma = N^2 k_c L_{\mathrm{bond}}^2 (\epsilon - \epsilon_{\mathrm{crit}})$. Substitution will make the equation dimensionless, yielding

$$\ddot{\Theta} = \nabla^2\Theta + \Theta - \Theta^3.$$

Let us pick a line of propagation for our solution and assume planar symmetry around this line. Then our equation reads:

$$\ddot{\Theta} = \partial_s^2\Theta + \Theta - \Theta^3, \quad \text{where} \quad s = \begin{pmatrix} n_x \\ n_y \\ n_z \end{pmatrix} \cdot \begin{pmatrix} \tilde{x} \\ \tilde{y} \\ \tilde{z} \end{pmatrix}, \quad \text{and} \quad \begin{pmatrix} n_x \\ n_y \\ n_z \end{pmatrix} = \hat{n} \text{ is a unit vector.}$$

This equation has known solutions of the form (7)

$$\Theta(\tilde{t}, s) = \pm \tanh\left(\frac{s - \tilde{a} + \tilde{v}\tilde{t}}{\sqrt{2\left(1 - \tilde{v}^2\right)}}\right),$$

where $\tilde{a}$ and $\tilde{v}$ are dimensionless space and velocity variables. Even for the static case, where $\tilde{v} = 0$, solutions are permitted and they have the form $\Theta = \pm \tanh\left(\left[s - \tilde{a}\right]/\sqrt{2}\right)$, which allow for the direction of buckling to be changed within certain planes. It thus proves that the emergence of domain walls as seen in the experiments (see Fig. 1*D*) are an allowed static solution of our system of equations.

Dynamical stability analysis. We would like to perform a stability analysis on the dynamical equation, considering only one angle to be non-zero and by neglecting cubic terms. Therefore,

$$J_I\ddot{\theta} + c_{\text{disp}}\dot{\theta} = \left(k_s L_{\text{bond}}^2 - k_b\right) L_{\text{bond}}^2 \nabla_{xz}^2\theta + k_t L_{\text{bond}}^2 \frac{\partial^2\theta}{\partial y^2} + N^2 k_c L_{\text{bond}}^2 \left[\epsilon - \epsilon_{\text{crit}}\right]\theta.$$

We can take the 4D Fourier transform to get:

$$J_I\omega^2 + ic_{\text{disp}}\omega = \left(k_s L_{\text{bond}}^2 - k_b\right) L_{\text{bond}}^2 \left(\kappa_x^2 + \kappa_z^2\right) + k_t L_{\text{bond}}^2 \kappa_y^2 - N^2 k_c L_{\text{bond}}^2 \left[\epsilon - \epsilon_{\text{crit}}\right],$$

with

$$\omega = \frac{-ic_{\text{disp}} \pm \sqrt{-c_{\text{disp}}^2 + 4J_I\left(\kappa_A^2 - m^2\right)}}{2J_I},$$

where $\kappa_A^2 = \left(k_s L_{\text{bond}}^2 - k_b\right) L_{\text{bond}}^2 \left(\kappa_x^2 + \kappa_z^2\right) + k_t L_{\text{bond}}^2 \kappa_y^2$ and $m^2 = N^2 k_c L_{\text{bond}}^2 \left[\epsilon - \epsilon_{\text{crit}}\right]$.

Depending on the value of the determinant the system is underdamped, overdamped, or critically damped. This depends both on the material properties, such as the damping factor, the energy of the wave, but also on the amount of strain that is applied.

When $c_{\text{disp}}^2 > 4J_I\left(\kappa_A^2 - m^2\right)$ the system is overdamped and the waves decay as exponentials. If $c_{\text{disp}}^2 = 4J_I\left(\kappa_A^2 - m^2\right)$ the system is critically damped and when $c_{\text{disp}}^2 < 4J_I\left(\kappa_A^2 - m^2\right)$ it is underdamped and waves oscillate while losing energy. Since $m^2 \sim \left[\epsilon - \epsilon_{\text{crit}}\right]$ it can change sign depending on the amount of strain that is applied. During post-buckling, when $\epsilon > \epsilon_{\text{crit}}$, the applied strain will cause the system to become more and more overdamped.

References

1. B Deng, J Raney, V Tournat, K Bertoldi, Elastic vector solitons in soft architected materials. *Phys. Rev. Lett.* **118**, 204102 (2017).
2. B Deng, P Wang, Q He, V Tournat, K Bertoldi, Metamaterials with amplitude gaps for elastic solitons. *Nat. Commun.* **9**, 3410 (2018).
3. C Mo, J Singh, JR Raney, PK Purohit, Cnoidal wave propagation in an elastic metamaterial. *Phys. Rev. E* **100**, 013001 (2019).
4. B Deng, S Yu, AE Forte, V Tournat, K Bertoldi, Characterization, stability, and application of domain walls in flexible mechanical metamaterials. *Proc. Natl. Acad. Sci.* **117**, 31002–31009 (2020).
5. B Deng, J Li, V Tournat, PK Purohit, K Bertoldi, Dynamics of mechanical metamaterials: A framework to connect phonons, nonlinear periodic waves and solitons. *J. Mech. Phys. Solids* **147**, 104233 (2021).
6. J Veenstra, et al., Non-reciprocal topological solitons in active metamaterials. *Nature* **627**, 528–533 (2024).
7. M Lizunova, J Van Wezel, An introduction to kinks in φ^4-theory. *SciPost Phys. Lect. Notes* p. 023 (2021).